# Detecting regional patterns of changing $CO_2$ flux in Alaska

Nicholas C. Parazoo[a,b,1], Roisin Commane[c,d], Steven C. Wofsy[c,d], Charles D. Koven[e], Colm Sweeney[f,g], David M. Lawrence[h], Jakob Lindaas[c,i], Rachel Y.-W. Chang[j], and Charles E. Miller[a]

[a]Jet Propulsion Laboratory, California Institute of Technology, Pasadena, CA 91109; [b]Joint Institute for Regional Earth System Science and Engineering, University of California, Los Angeles, CA 90095; [c]Department of Earth and Planetary Sciences, Harvard University, Cambridge, MA 02138; [d]Harvard School of Engineering and Applied Sciences, Harvard University, Cambridge, MA 02138; [e]Climate and Ecosystem Sciences Division, Lawrence Berkeley National Laboratory, Berkeley, CA 94720; [f]National Oceanic and Atmospheric Administration/Earth System Research Laboratory, Boulder, CO 80305; [g]Cooperative Institute for Research in Environmental Sciences, University of Colorado, Boulder, CO 80309; [h]Climate and Global Dynamics Laboratory, National Center for Atmospheric Research, Boulder, CO 80302; [i]Department of Atmospheric Science, Colorado State University, Fort Collins, CO 80523; and [j]Department of Physics and Atmospheric Science, Dalhousie University, Halifax, NS, Canada B3H 4R2

Edited by Inez Y. Fung, University of California, Berkeley, CA, and approved May 17, 2016 (received for review January 20, 2016)

**With rapid changes in climate and the seasonal amplitude of carbon dioxide ($CO_2$) in the Arctic, it is critical that we detect and quantify the underlying processes controlling the changing amplitude of $CO_2$ to better predict carbon cycle feedbacks in the Arctic climate system. We use satellite and airborne observations of atmospheric $CO_2$ with climatically forced $CO_2$ flux simulations to assess the detectability of Alaskan carbon cycle signals as future warming evolves. We find that current satellite remote sensing technologies can detect changing uptake accurately during the growing season but lack sufficient cold season coverage and near-surface sensitivity to constrain annual carbon balance changes at regional scale. Airborne strategies that target regular vertical profile measurements within continental interiors are more sensitive to regional flux deeper into the cold season but currently lack sufficient spatial coverage throughout the entire cold season. Thus, the current $CO_2$ observing network is unlikely to detect potentially large $CO_2$ sources associated with deep permafrost thaw and cold season respiration expected over the next 50 y. Although continuity of current observations is vital, strategies and technologies focused on cold season measurements (active remote sensing, aircraft, and tall towers) and systematic sampling of vertical profiles across continental interiors over the full annual cycle are required to detect the onset of carbon release from thawing permafrost.**

carbon cycle | permafrost thaw | climate | Earth system models | remote sensing

The future trajectory of carbon balance in the Arctic–Boreal Zone (ABZ) is of global importance because of the vast quantities of carbon sequestered in permafrost soils (1). Climate warming threatens to increase permafrost thaw and release soil carbon back to the atmosphere as a positive feedback promoting additional warming (2). It is unclear whether the observed intensification of the northern high-latitude carbon cycle is dominated by plant productivity or microbial decomposition, both of which seem to be increasing (3–6). Although warming temperatures and C/N fertilization promote greening and higher summer productivity during the short, intense growing season, these same factors also drive increased emissions during the long cold season (3–5).

Detecting changes in ABZ carbon balance requires sustained observations over the full annual cycle. In the last decade, researchers have recognized the importance of year-round land–atmosphere $CO_2$ flux observations (3–5). Synthesis studies of these data show that increasing growing season uptake has been offset by stronger winter respiration. Measurements of atmospheric $CO_2$ collected from in situ and remote sensing instruments provide spatially and temporally integrated constraints of net $CO_2$ exchange on regional to pan-Arctic scales. In situ observations have been limited primarily to a small network of surface towers and infrequent, short duration airborne campaigns designed primarily to detect the pan-Arctic background $CO_2$ signal but have provided key evidence of ongoing large-scale changes in the structure and metabolism of the ABZ (6–9). Airborne observations show a trend of increasing $CO_2$ seasonal cycle amplitude (difference between maximum spring $CO_2$ and minimum summer $CO_2$) (7), with additional analysis suggesting that enhancements in growing season photosynthetic intensity and summer uptake in boreal regions are the most likely source of amplification (8). Ground-based measurements of high-latitude background air show a trend toward earlier $CO_2$ buildup in fall, suggesting a shorter carbon uptake period (9). The ABZ, thus, seems to be transitioning toward both increased uptake early in the growing season and increased respiration in the cold season.

Despite these advances, several factors have limited the ability of current atmospheric $CO_2$ observing strategies to fully constrain ABZ carbon balance changes. (*i*) Background variability: long-range $CO_2$ transport from lower latitudes drives much of the high-latitude seasonal cycle (10, 11) and obscures local signals. (*ii*) Interannual variability: short-term $CO_2$ variability driven by year to year changes in ABZ carbon balance and long-range transport obscures slower, long-term changes driven by climate warming. (*iii*) Limited near-surface coverage: the $CO_2$ content of air above 3 km [~700 millibars (mb)] and poleward of 60° N is influenced primarily by processes in northern midlatitudes (30° N to 60° N), including a strong terrestrial influence in summer (12). Observations at altitudes above 4 km (e.g., 500 mb) are only weakly sensitive to the ABZ. (*iv*) Limited spatial coverage: the ABZ is characterized by strong spatial heterogeneity in plant functional type, permafrost

## Significance

**Dramatic warming in northern high latitudes has led to increased photosynthetic carbon uptake during the short, intense growing season; however, microbial decomposition of soil carbon and increased emissions during the long cold season may offset summer uptake and impart a positive feedback on the global climate system. We show that current airborne and satellite measurements of atmospheric $CO_2$ can accurately quantify summer uptake but are insufficient to detect regional changes in cold season emissions. As the potential for Arctic carbon budgets to become impacted by permafrost thaw and cold season emissions increases, strategies focused on year-round vertical profiles and improved spatial sampling will be needed to track carbon balance changes.**

Author contributions: N.C.P., S.C.W., C.D.K., and C.E.M. designed research; N.C.P. performed research; R.C., C.D.K., C.S., D.M.L., J.L., R.Y.-W.C., and C.E.M. contributed new reagents/analytic tools; N.C.P. analyzed data; and N.C.P. wrote the paper.

The authors declare no conflict of interest.

This article is a PNAS Direct Submission.

Data deposition: The data reported in this paper have been deposited in the Oak Ridge National Laboratory Distributed Active Archive Center, Oak Ridge (dx.doi.org/10.3334/ORNLDAAC/1325).

[1]To whom correspondence should be addressed. Email: nicholas.c.parazoo@jpl.nasa.gov.

This article contains supporting information online at www.pnas.org/lookup/suppl/doi:10.1073/pnas.1601085113/-/DCSupplemental.

extent, and climate (13). Spatial sampling with significantly greater density than available from current ground-based and aircraft observing systems is needed. (*v*) Limited seasonal coverage: climate warming has intensified seasonal carbon exchange in the ABZ, with increasing summer uptake offset by increasing winter emissions (3–6). Observations restricted to the growing season fail to capture this differential temporal response, such that key drivers of present and future carbon balance may go undetected.

Based on these limitations, $CO_2$ observations collected at multiple temporal (seasons and years) and spatial (horizontal and vertical) scales are needed for more accurate detection of regional carbon cycle changes in the ABZ. Here, we investigate seasonal carbon fluxes in Alaska using satellite and airborne observations from 2009 to 2013. We leverage remote sensing observations from the Greenhouse Gases Observing Satellite (GOSAT), airborne in situ observations from the Carbon in Arctic Reservoirs Vulnerability Experiment (CARVE) and National Oceanic and Atmospheric Administration (NOAA) Arctic Coast Guard (ACG) flights, and weekly NOAA airborne vertical profile measurements at Poker Flat, AK (PFA) (see dx.doi.org/10.3334/ORNLDAAC/1325). Together, these measurements sample vertically resolved and column-averaged $CO_2$ dry air mole fractions ($XCO_2$) across the full annual cycle and contain sustained multiyear information spanning local, regional, and pan-Arctic spatial scales (Figs. S1, S2, and S3). We compare these data with atmospheric simulations driven by modeled terrestrial carbon fluxes for present and future climate to distinguish local biological processes from background variability and determine detectability of future carbon–climate feedbacks associated with permafrost thaw.

## Materials and Methods

CARVE, ACG, PFA, and GOSAT datasets are described briefly here and in more detail in *S1: Observed $CO_2$*. CARVE campaign flights were conducted for periods of 2 wk/mo from May to September of 2012 and from April to October of 2013, with 4–10 flights per campaign and 75 total tracks collected from 2012 to 2013 (Fig. S1). CARVE surveys focus on the lowest 500 m above the surface, with frequent vertical profiles. ACG flights collect high-resolution $CO_2$ in situ concentration data across more than 50 flights and an average of three vertical profiles per flight from 2009 to 2013 from early March to late November (Fig. S2). ACG typically measures vertical profiles over boreal and Arctic Alaska on the same day. PFA is based on year-round, fixed location, high-resolution airborne $CO_2$ flask concentration data collected at 12 different altitudes [500–8,000 m above sea level (asl)] over the PFA Research Range northeast of Fairbanks, AK every 2–4 wk since 2000. GOSAT $XCO_2$ retrievals have produced full coverage of the growing season (April to September) and partial coverage of spring and fall shoulder seasons at Alaska to pan-Arctic scales since 2009 (Fig. S3).

All aircraft datasets are filtered for biomass burning using onboard CO measurements and a high CO screen of 150 parts per billion (ppb) and then, separated into mixing layer (ML) and free troposphere (FT) bins to examine local vs. long-range effects on $CO_2$ seasonality. We consider several factors in choosing the altitude to separate these layers. Comparison of 1-km bins from 0 to 7 km shows high sensitivity of vertical gradients to year, season, and dataset (Fig. S4 *A–C*). The level at which the ML is decoupled from the FT also varies but typically resides at 2–4 km. In general, the vertical gradient exhibits very similar seasonal structure independent of choice of averaging bins (Fig. S4 *D* and *E*). For this analysis, we choose 3 km, because it represents the highest daily extent of the layer of surface influence and the pressure level (700 mb) above which air from midlatitudes has the strongest influence (12). We average all available data in the lowest 3 km asl (>700 mb) for the ML and from 3 to 7 km asl (700–500 mb) for the FT, noting that the approximate ML sampling altitude below 3 km varies across datasets. We use all available airborne data from 8:00 AM to 8:00 PM local standard time (LST), but most data were collected from midday to 4:00 PM. We note a slight sensitivity of the vertical distribution and gradient of the $CO_2$ seasonal cycle to diurnal sampling biases (Fig. S5), which are likely attributed to diurnal variability in $CO_2$ flux and ML depth. We remove the secular trend and calculate spring and fall zero crossing dates as discussed in *S1: Observed $CO_2$*.

We simulate atmospheric $CO_2$ using the Goddard Earth Observing System Chemistry global tracer model (GEOS-Chem) (14) forced by assimilated meteorological fields and surface $CO_2$ flux from land, ocean, and fossil fuel sources. Monthly $CO_2$ output is sampled during midday (10–18 LST), averaged across all Alaskan land grid points (55° N to 72° N, 170° W to 140° W), and binned vertically into the ML and FT. We run $CO_2$ experiments based on two configurations of the Community Land Model, version 4.5 (CLM4.5) (15–17). These experiments are described briefly below and in more detail in *S2: Land and Atmospheric Simulations*.

The first experiments, denoted TRANSPORT, focus on the present day (2009–2013) to examine sensitivity of observed $CO_2$ seasonal cycles to Alaskan $CO_2$ flux. These simulations use year-specific CLM4.5 flux (18) and winds to best represent observed conditions and interannual variability. Three variants are considered: (*i*) CONTROL, a baseline run with all fluxes turned on; (*ii*) ALASKA-OFF, an Arctic influence run with Alaskan fluxes at zero for the domain (55° N to 72° N, 170° W to 140° W); and (*iii*) ARCTIC-OFF, the long-range transport run with Arctic fluxes set to zero for the domain (55° N to 90° N, 180° W to 180° E).

The second set of experiments focuses on the ability of current observing strategies to detect changes in $CO_2$ flux patterns resulting from projected climate-induced changes in the ABZ carbon cycle. These simulations use time-varying winds from 2000 to 2010 and six sets of decadal CLM4.5 fluxes for present day (HIST, 1990–2010) and future (15YR, 2005–2015; 30YR, 2020–2030; 50YR, 2040–2050; 100YR, 2090–2100; 200YR, 2190–2200) scenarios. Present day and future scenarios are further divided into simulations to test $CO_2$ sensitivity to flux changes in Alaska (ALASKA-ON), in the Arctic (ARCTIC-ON), and at global scale (GLOBAL-ON). CLM4.5 is configured as described in two recent permafrost studies (19, 20) and forced by time-varying meteorology corresponding to historical and future climates (Fig. S6 and *S2: Land and Atmospheric Simulations*), with modeled photosynthesis driven by constant preindustrial $CO_2$. We consider two scenarios for permafrost thaw. The first, denoted FUTURE-DEEP, assumes that deep permafrost carbon is active (19). In the second, denoted FUTURE-SHALLOW, deep soil decomposition is disabled by varying a parameter $Z_\tau$ in CLM4.5, which controls decomposition rates as a function of soil depth. These experiments decouple changing dynamics of surface soils from deep soils and isolate the potential contributions from permafrost layers (19).

## Results and Discussion

**Observing $CO_2$ Signals over Alaska.** Alaskan airborne and satellite datasets show a similar range of seasonal and interannual variability throughout the ML, FT, and column but exhibit key differences in seasonal cycle amplitude and phase in the multiyear average and throughout the vertical column (Fig. 1 *A–C*, Fig. S7, and *S1: Observed $CO_2$*), including a wide range of dates for spring and fall zero crossing and amplitudes of spring enrichment and summer depletion. These differences are attributed to the range of

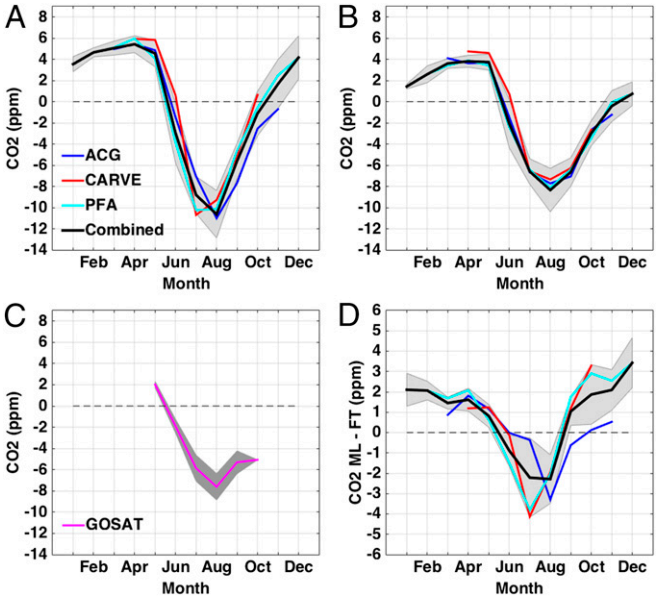


**Fig. 1.** Observed $CO_2$ seasonal cycles from satellite and airborne instruments. Shown are individual (color) and combined (black) observations averaged from 2009 to 2013 for (*A*) FT (3–7 km asl), (*B*) ML (0–3 km asl), (*C*) column average, and (*D*) vertical gradient (difference between ML and FT). Shading is the monthly SD and represents interannual variability over 5 y. Values are monthly averages, and grid lines represent middle of month.

sampling strategies used. For example, PFA resolves the full annual cycle but with low spatial sampling (essentially a fixed point), whereas ACG and CARVE have high spatial sampling but different footprints throughout the ML and FT (Figs. S1 and S2). ACG, CARVE, and GOSAT provide spatial sampling across the growing season and transition seasons but with reduced sampling during transition seasons. Compared with ACG, CARVE samples at higher spatial resolution, at lower average altitude in the ML and FT, and with a footprint focused more on the Alaskan interior, leading to different summer drawdown patterns. However, ACG, PFA, and GOSAT sample over multiple consecutive years (2009–2013), whereas this study only used CARVE data from 2012 to 2013. These results suggest that current airborne and satellite strategies capture key aspects of the Alaskan carbon cycle but that individual campaigns are unlikely to constrain regionally and seasonally integrated carbon balance changes because of the wide range of spatial and temporal variability throughout the ML and FT.

Averaging across airborne datasets from 2009 to 2013 combines the strengths of each observing strategy to better characterize seasonal carbon cycle behavior (Fig. 1 and Fig. S8*A*). The composite shows a linear decrease in seasonal cycle amplitude from 17.4 ± 3.5 parts per million (ppm) in the ML to 13.6 ± 3.5 ppm in the FT and lengthening of net carbon uptake period (time between spring and fall zero crossing) from 137 ± 16.4 d to 159 ± 9.24 d through delayed fall zero crossing at larger spatial scales (increasing spatial footprint). Column data from GOSAT show a similar pattern of reduced seasonal cycle amplitude, longer growing season carbon uptake period, and delayed fall zero crossing moving to progressively larger spatial scales (Alaska, pan-Arctic, and midlatitudes). In contrast, spring zero crossing dates show minimal variability (within 2 d) across airborne and satellite datasets.

Despite improved representation of regional carbon cycle changes in Alaska in combined airborne data, TRANSPORT simulations indicate that $CO_2$ signals in the ML, FT, and column are strongly masked by long-range transport from both the pan-Arctic and lower latitudes (*S3: Long-Range Transport*). For example, the large observed difference in zero crossing dates in fall relative to the small difference in spring zero crossing is a function of the difference between the transport and Alaskan components of seasonal cycle amplitude. Spring source–sink transition occurs earlier in midlatitudes than at high latitudes, but transport delays propagation of midlatitude signals to Alaska, such that the ML and FT experience spring depletion at the same time. In contrast, the fall sink–source transition occurs earlier at high latitudes, whereas transport delays midlatitude signals, thus leading to the large timing difference in fall zero crossing days in the ML and FT. TRANSPORT runs that zero $CO_2$ fluxes in Alaska (ALASKA-OFF) and pan-Arctic (ARCTIC-OFF) show delays of 1 and 2 wk, respectively, in fall zero crossing relative to CONTROL. These runs also suggest that Alaskan fluxes contribute less than 10% to observed seasonal amplitude over Alaska (*S3: Long-Range Transport*) (11, 12).

We find that the $CO_2$ vertical gradient, defined as the difference between ML and FT $CO_2$, gives a robust measure of Alaskan $CO_2$ fluxes, because subtracting FT from ML $CO_2$ reduces the influence of long-range transport. In combined airborne observations, the seasonal amplitude of the vertical gradient is 4–5 ppm (Fig. 1*D*). Peak depletion in the $CO_2$ vertical gradient occurs by or before August, similar to ML and FT $CO_2$, but has more rapid enrichment and earlier zero crossing in fall, indicative of a stronger local influence. Comparing individual airborne datasets shows earlier and deeper spring drawdown and more rapid fall enrichment in CARVE and PFA compared with ACG. CONTROL reproduces key seasonal (Fig. 2*A*) features of combined observations, including seasonal amplitude, zero crossing dates, and peak summer depletion, and interannual features during summer attributed to variations in $CO_2$ flux ($r$ = 0.88 ± 0.28) (Fig. S9). The timing and magnitude of simulated spring depletion are more consistent with CARVE and PFA than ACG. This anomaly in ACG is likely the result of sparse sampling in the Alaskan ML (Fig. S2), which reduces sensitivity to Alaskan $CO_2$ fluxes, and highlights the importance of spatially distributed airborne sampling in the continental interior ML.

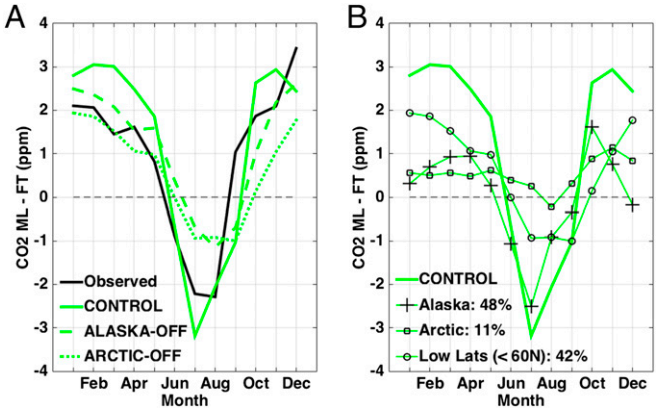


**Fig. 2.** Sensitivity of $CO_2$ vertical gradient to long-range transport vs. Alaskan $CO_2$ flux. (*A*) Observed (black) and simulated (green) seasonal cycles. Observations are based on combined airborne datasets from Fig. 1*D*. Simulations are based on TRANSPORT experiments for CONTROL (solid), ALASKA-OFF (dashed), and ARCTIC-OFF (dotted). (*B*) Regional contributions to CONTROL (solid) for Alaska (+), pan-Arctic (□), and low latitudes (○) estimated as the difference between TRANSPORT experiments in *A*. Lines represent seasonal average from 2009 to 2013.

Degradation of simulated amplitude and phase in ALASKA-OFF and ARCTIC-OFF supports a strong contribution of Alaskan $CO_2$ fluxes to observed vertical gradients in Alaska. We estimate that 48% of the CONTROL amplitude is driven locally (CONTROL − ALASKA-OFF) compared with 11% from the pan-Arctic (CONTROL − ARCTIC-OFF) and 41% from low latitudes (ARCTIC-OFF) (Fig. 2*B*). Taken together, we find that Alaskan fluxes drive a short but intense carbon uptake period, with $CO_2$ depletion in early summer and enrichment in late summer to early fall. These fluxes are subject to interannual variations driven by observed climate anomalies (13), which are reflected in vertical $CO_2$ gradients (Fig. S9), highlighting a need for year-round airborne profiles sustained over multiple consecutive years to disentangle rapid changes in uptake from slow persistent changes.

**Detecting Future Carbon Balance Signals.** The experiments above show that Alaskan $CO_2$ fluxes produce observable signals in the vertical gradient of atmospheric $CO_2$. Given trends of intensifying seasonal $CO_2$ amplitude since 1960 (7) and projected intensification with climate warming (19), a critical question is how future climate-induced ABZ carbon cycle changes will manifest themselves and whether these changes produce $CO_2$ signals that are detectable in the presence of interannual variability. We investigate the detectability of climate-induced carbon balance changes by analyzing $CO_2$ vertical gradients forced by CLM $CO_2$ flux projections. We focus our analysis on the response to changing climate in the absence of the confounding effect of carbon fertilization, which leads to large differences in uptake depending on nutrient limitation (19), although we also show patterns in the presence of this effect (Fig. S6).

Climate change simulations with an active deep permafrost carbon layer (FUTURE-DEEP) indicate a slight increase in total annual emissions in Alaska from near carbon-neutral conditions in 1990–2010 to a moderate source (0.05 Pg C $y^{-1}$) in 15–50 y and a strong source (0.15 Pg C $y^{-1}$) in 100–200 y and strong amplification of seasonal exchange, with earlier spring uptake, stronger summer uptake, earlier/stronger fall/winter emissions, and a shift of peak emissions from September to October (Fig. 3*A*) as the phase lag of heat conduction shifts decomposition of deep soil carbon later into fall and winter (19).

Atmospheric simulations driven by projected $CO_2$ flux changes in Alaska and fluxes outside Alaska fixed to the period 1990–2000 (ALASKA-ON) show corresponding increases in the seasonal amplitude (fall − summer) of Alaskan $CO_2$ vertical gradients (Fig. 3*B*),

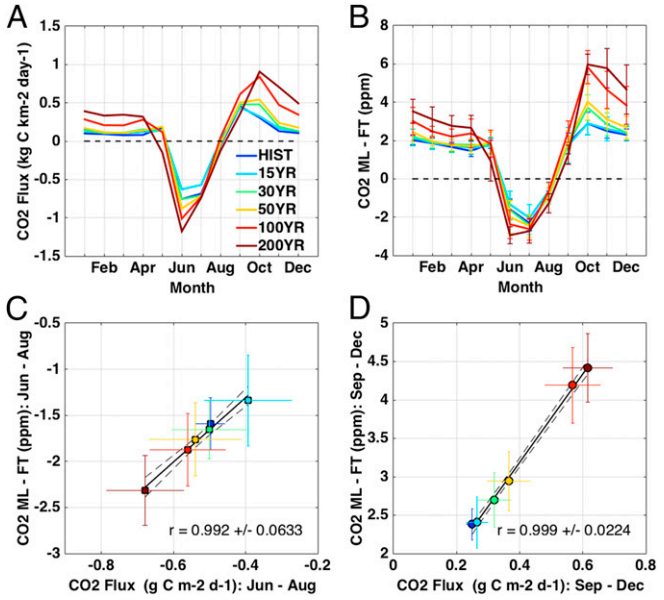


**Fig. 3.** Modeled $CO_2$ sensitivity to future warming and permafrost thaw. (*A*) CLM4.5 $CO_2$ flux for projected warming scenarios in Alaska: HIST (1990–2000; dark blue), 15YR (2005–2015; light blue), 30YR (2020–2030; green), 50YR (2040–2050; yellow), 100YR (2090–2100; light red), and 200YR (2190–2200; dark red). (*B*) $CO_2$ vertical gradient for warming scenarios in *A*. (*C*) Regression of $CO_2$ vertical gradient summer minimum (June to August) against summer $CO_2$ flux. (*D*) Same as *C* but for fall (September to December).

rising from 3.97 ± 0.36 ppm initially to 6.73 ± 0.61 ppm in 2200. Enhanced summer depletion (stronger negative gradient) is correlated with increased uptake from June to August (Fig. 3*C*), and enhanced fall enrichment (stronger positive gradient) is correlated with increased emissions from September to December (Fig. 3*D*). Summer signals show reduced depletion over the first 15 y as respiration outpaces photosynthesis and then, enhanced depletion as growing conditions improve in 15–200 y. Fall $CO_2$ signals increase slowly at first (0–50 y) as decomposition of deep soil carbon is delayed by low liquid moisture and oxygen availability and then, more rapidly (50–200 y) after initial active layer deepening is established.

A key result is that climate-induced $CO_2$ signals increase more rapidly (relative to HIST) and significantly (compared with interannual variability) in fall than summer. Comparing the months of strongest enrichment (October) with those of strongest depletion (June) shows a factor of three stronger change over 50 y (50YR − HIST; fall $CO_2$ increase of 1.14 ± 1.12 ppm vs. summer decrease of 0.41 ± 1.0 ppm), a factor of four stronger change over 100 y (100YR − HIST; 2.94 ± 1.04 ppm vs. 0.79 ± 0.92 ppm), and a factor of two stronger change over 200 y (200YR − HIST; 3.08 ± 0.79 ppm vs. 1.35 ± 0.70 ppm). Strong $CO_2$ interannual variability is likely to mask most of the summer signal over the next 100 y, whereas regional-scale changes in fall may be detectible in as early as 30 y (30YR − HIST = 0.83 ± 0.89 ppm in October). These results indicate that a hypothetical observing system, with perfect spatial and temporal sampling over Alaska, has high likelihood of detecting projected slow regional carbon balance impacts in fall in the next 30–50 y and low likelihood of detecting summer impacts over the next 200 y.

To test the ability of current observing systems to detect predicted carbon balance changes given known temporal and spatial sampling limitations, we sample simulated $CO_2$ concentrations in 100YR based on the timing and methods of CARVE, PFA, ACG, and GOSAT observations collected in 2012. We then compare the corresponding, subsampled "observed" mean with the "true" mean calculated from sampling all Alaskan land points (Fig. 4*A*). Current airborne and satellite sampling strategies capture general patterns of enhanced summer depletion and cold season enrichment in 100 y. However, airborne strategies show a range of variability in the depth and timing of summer $CO_2$ depletion, leading to biases in estimates of regional mean drawdown from April to September, which are smallest for CARVE sampling [root mean square error (RMSE) = 0.23 ppm] and largest for PFA (RMSE = 0.38 ppm). Spring and fall transitions represent periods of largest spreads across sampling strategies. PFA, the only system to measure continuously through the entire cold season, shows increased bias in winter (RMSE = 0.76 ppm). All strategies, including GOSAT, capture but underestimate peak enrichment in October. In general, the combined airborne strategy reduces bias during overlapping sampling from April to October (RMSE = 0.24 ppm), with the largest improvements during the growing season (June to August) but with cold season sampling biases that underestimate fall respiration (September to October) and overestimate winter respiration (December to March).

Spatial gradients have an important influence on detection of regional $CO_2$ fluxes by the current observing network. Summer fluxes, with a relatively modest ∼1 ppm southwest to northeast positive $CO_2$ gradient (Fig. 4*C*) driven by increasing emissions in northeast Alaska and increased uptake in southwest Alaska (Fig. S10*A*), are well-characterized by the spatially diverse set of airborne and satellite strategies. Conversely, winter shows spatially homogenous increases in emissions across western and northern Alaska (Fig. S10*B*) but locally strong $CO_2$ vertical gradients north of the Brooks Range along the North Slope (4 ppm relative to annual mean) (Fig. 4*D*). These gradients are likely enhanced by shallow winter MLs, and CLM4.5 shows potential for additional enhancement by increased fall respiration associated with $CO_2$ fertilization (Fig. S6*B*). These results suggest that future cold season emissions in the interior North Slope may go unobserved by the 2012 observing network, despite measurements by ACG along the north coast (Fig. S2*D*) and PFA in central Alaska because of low sensitivity of current observations to this region.

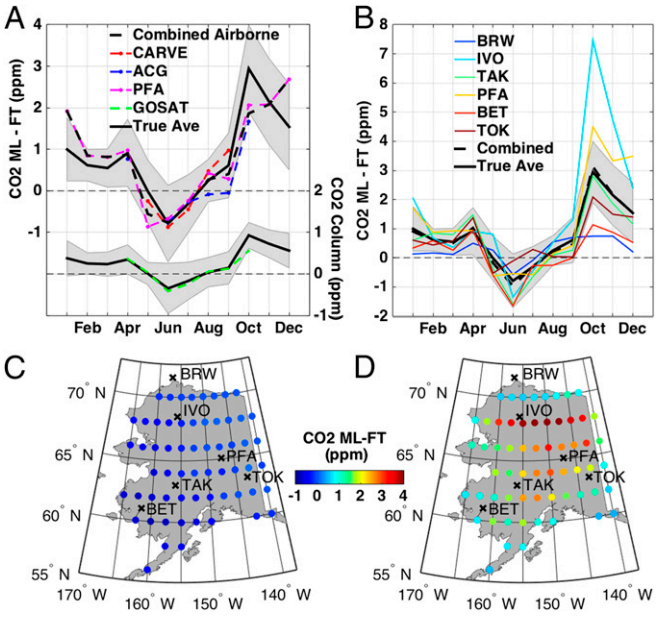


**Fig. 4.** Hypothetical $CO_2$ seasonal cycle changes based on CARVE, ACG, and PFA sampling under future warming scenarios. (*A*) Difference in $CO_2$ vertical gradient seasonal cycle between 100YR and HIST (100YR − HIST) based on the average of all Alaskan grid points [solid black, true average (True Ave)] and grid points likely to be sampled based on current airborne (red, CARVE; blue, ACG; magenta, PFA), satellite (green, GOSAT), and combined airborne (dashed black) strategies. (*B*) Same as *A* but for the theoretical network of fixed point airborne flask locations shown in *C* and *D*. (*C*) Map of *A* for summer average (June to August). (*D*) Map of *A* for fall average (September to December). BET, Bethel; IVO, Ivotuk; TAK, Takotna; TOK, Tok.

These results argue for a more strategic, spatially distributed observing network that samples the full annual cycle to ensure detection of changing cold season emissions and resolve annual carbon budgets. The existing network of "stationary" sites includes PFA and two tall tower sites not analyzed in this paper: the Barrow (BRW) tower along the North Slope coast and the CARVE (CRV) tall tower north of Fairbanks, AK. These tower sites have been running since 1973 and 2011, respectively, delivering key long-term, continuous (approximately hourly), high-density measurements in the ML needed to fill 2-wk sampling gaps and provide a temporal context for airborne data (21). However, the calculated footprints of these sites indicate that portions of western and eastern Alaska and the North Slope uplands have very little influence on these observations.

Considering the relative affordability and seasonal continuity of fixed point airborne sampling relative to intensive campaigns, such as CARVE, we test strategies for augmented airborne airborne vertical profiles to fill spatial gaps poorly sampled by the PFA–CRV–BRW network. We consider a network with five additional airborne vertical profile locations sampling at regular 2-wk intervals from the surface to 8 km (~500 mb) and distributed across Alaska (Fig. 4 *B–D*) at locations with existing and/or historical measurements (tall tower, flux tower, or airborne campaigns) and infrastructure (airports and cell phone towers). BRW and Ivotuk represent the North Slope coast and upland tundra, respectively. Bethel and Takotna represent the Yukon Delta and western interior, respectively. PFA represents the continental interior, and Tok provides a background site in the eastern interior.

The signals from the augmented network of fixed point airborne sites exhibit significant variability from October to December, but together, they capture mean patterns of summer drawdown and cold season emissions with negligible bias (Fig. 4*B*). The Ivotuk site (or any upland tundra site along the southern edge of the North Slope) provides a key source of new information for the North Slope tundra and captures a factor of two greater local fall respiration enrichment compared with the regional mean (7.2 vs. 3.0 ppm in October), suggesting a strong likelihood for detecting local changes on earlier timescales (0–30 y) than at regional scales (30–50 y), especially in the case of respiration amplified by $CO_2$ fertilization. The coastal sites BRW and Bethel as well as Tok constrain continental and background air entering Alaska and may help to identify changing source regions under changing atmospheric transport regimes.

Dedicated carbon observing satellites, such as GOSAT, provide essential geographical coverage within Alaska and at the pan-Arctic scale that is missing or poorly sampled by sparse tall tower and airborne measurements. However, GOSAT, Orbiting Carbon Observatory-2, and other satellites that rely on passive near-IR techniques for measuring total column $CO_2$, including missions using highly elliptical orbits to obtain dense high-latitude sampling (22), require sunlight reflected from the Earth's surface and thus, return poor sample yield during the long, dark cold season. Even for cold season measurements, passive IR techniques are challenged by signals in large air masses because of high solar zenith angles. Thermal IR sounders, such as Atmospheric Infrared Sounder, Infrared Atmospheric Sounding Interferometer, and Thermal Emission Spectrometer, provide year-round coverage but sample the mid- to upper troposphere (700–500 mb) and do not provide ML sensitivity (23). Active $CO_2$ sensors (24) offer promise for year-round performance in high latitudes but have not yet shown the required precision or technical maturity for long-term ground-, airborne-, or space-based deployment.

Further complicating carbon balance detectability for satellite, airborne, and surface measurements is that climate change outside Alaska is likely to drive $CO_2$ flux changes that obscure Alaskan signals. Warming scenarios in CLM4.5 drive increased summer uptake and winter emissions across the pan-Arctic but opposite changes in midlatitudes, including reduced summer uptake and winter emissions (Fig. S10 *A* and *B*). Compared with ALASKA-ON, pan-Arctic climate change (ARCTIC-ON) drives an additional 0.3–0.8 ppm summer $CO_2$ depletion and 2–3 ppm winter enrichment (Fig. S10 *C* and *D*). Global climate change (GLOBAL-ON) drives an additional 1 ppm summer depletion, despite reduced uptake in lower latitudes, with negligible changes in winter enrichment (Fig. S10*E*). However, increased summer depletion is an artifact of $CO_2$ vertical gradients, where transport from reduced uptake regions in lower latitudes leads to a lower rate of FT $CO_2$ depletion compared with the ML (Fig. S10*H*). Thus, the influence of confounding climate effects from multiple source regions demands analysis of separate FT and ML changes as a context to interpret vertical gradients. Our results strongly argue for use of year-round airborne vertical profiles as an important constraint for regional carbon balance changes.

**Detecting Emerging Carbon Sources.** Analysis of permafrost carbon–climate feedback indicates that the permafrost region is highly sensitive to the decomposition of subsurface permafrost layers, with climate driven losses across the pan-Arctic by the year 2200 totaling 71–166 Pg C depending on the decomposability of deep carbon (19). In the weak carbon loss scenario (~0.5 m), deep layers remain undecomposed, with respiration limited to shallow soils. For strong carbon loss, deeper permafrost carbon (~10 m) is much more vulnerable to decomposition on warming. Because the processes controlling the rate and extent of deep permafrost thaw are highly uncertain, models cannot project the timing or magnitude of permafrost carbon release accurately (19, 25, 26). Therefore, $CO_2$ observing strategies designed to monitor changes in Arctic respiration patterns will be needed to avoid the risk of emerging permafrost carbon sources going undetected.

We test whether hypothetical airborne $CO_2$ observing strategies with continuous spatial and temporal sampling can distinguish surface from subsurface exchange to detect permafrost losses across the pan-Arctic by comparing $CO_2$ seasonal cycles for FUTURE-SHALLOW ($Z_\tau$ = 0.5 m) and FUTURE-DEEP ($Z_\tau$ = 10 m) for pan-Arctic–scale emissions (ARCTIC-ON). Differences in summer sink strength between these scenarios are negligible because of the seasonal delay of thermal diffusion to deeper soils but lead to stronger fall emissions in FUTURE-DEEP (Fig. S6). The projected $CO_2$ response shows similar summer depletion in HIST, 15YR, 30YR, and 50YR (Fig. 5 *A–D*) and slightly enhanced depletion in 100YR and 200YR (Fig. 5 *E* and *F*); however, these signals are not significantly different from each other because of low signal to noise, and they do not change significantly as the ABZ evolves to a warmer world.

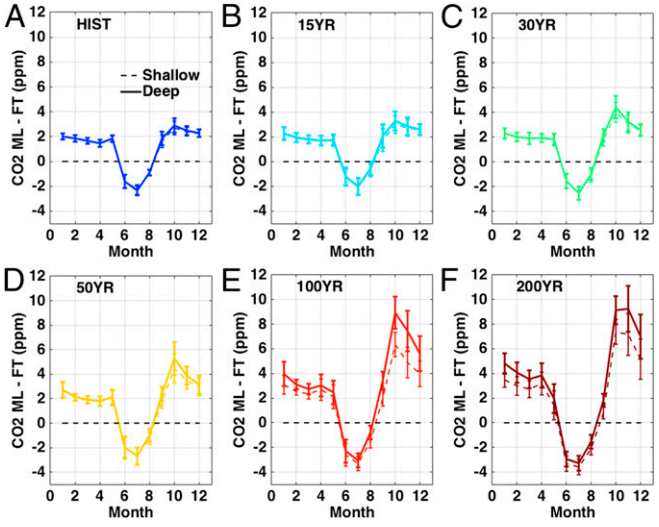


**Fig. 5.** $CO_2$ seasonal cycle changes in Alaska for shallow and deep permafrost carbon emission scenarios. $CO_2$ vertical gradient for FUTURE-SHALLOW (dashed lines) and FUTURE-DEEP (solid lines) permafrost scenarios shown for (*A*) HIST, (*B*) 15YR, (*C*) 30YR, (*D*) 50YR, (*E*) 100YR, and (*F*) 200YR based on experiments with pan-Arctic fluxes turned on (ARCTIC-ON).

Fall enrichment is similar until 100YR, after which signals caused by deep permafrost loss increase significantly compared with shallow loss, including 2.0- to 2.5-ppm difference from October to December.

These results suggest that the current airborne strategies are unlikely to disentangle signals from shallow and deep soil emissions in summer but could potentially detect deep permafrost carbon emissions in fall with improved temporal and spatial sampling. However, simultaneous respiration of shallow surface carbon and amplification by $CO_2$ fertilization and fire emissions is likely to mask deep permafrost emissions from a $CO_2$ observing system. Radiocarbon data, which can be used to partition respiration into autotrophic and heterotrophic young and old soil components (27), may provide a viable solution to disentangle and track future emissions from deep permafrost.

## Conclusions

The seasonal amplitude of $CO_2$ has been increasing in northern high latitudes over the past five decades (7). The ability to quantify ABZ contributions has been limited by the lack of long-term atmospheric $CO_2$ observations with sufficient temporal, vertical, or spatial resolution to constrain annual carbon budgets at the regional scale. Current airborne and satellite strategies are beginning to address some of these shortcomings with close monitoring of changing sink activity in the growing season. However, emerging carbon–climate feedbacks driven by warming, $CO_2$ fertilization, and fires are likely to reshape our understanding of the Arctic carbon cycle, such that earlier and stronger sinks are offset by enhanced sources. $CO_2$ and $CH_4$ emissions related to permafrost thaw and increasing biotic activity are unlikely to manifest themselves until later in the cold season (20, 28), shifting the ABZ to an irreversible carbon source that would go undetected by current sampling strategies and measurement systems until long after the onset of permafrost thaw.

The evolving ABZ biosphere and threat of unobserved cold season emissions call for a more comprehensive observing system focused on (*i*) year-round, (*ii*) vertically resolved, and (*iii*) spatially distributed sampling. Our analysis indicates that these three key objectives can be met by a network of airborne vertical profiles distributed across Alaska; however, the combination of tall tower continuous measurements, intensive airborne campaigns, and satellite remote sensing can significantly augment this network by providing temporal and spatial context. Based on existing technology and operating costs, we expect that a network of airborne profiles complemented by tall towers and satellite remote sensing will ensure that emerging carbon sources and sinks do not go undetected.

**ACKNOWLEDGMENTS.** Some of the research described was performed for CARVE, an Earth Ventures (EV-1) investigation, under contract with NASA. A portion of this research was carried out at the Jet Propulsion Laboratory, California Institute of Technology under a contract with NASA. C.D.K. was supported by the Director, Office of Science, Office of Biological and Environmental Research (BER) of the US Department of Energy (DOE) Contract DE-AC02–05CH11231 as part of their Regional and Global Climate Modeling (BGC-Feedbacks SFA) and Terrestrial Ecosystem Science (NGEE-Arctic) Programs. D.M.L. was supported by the US DOE, BER as part of Climate Change Prediction Program Cooperative Agreement DE-FC03-97ER62402/A010 and by NSF Grant PLR-1304220.

1. Tarnocai C, et al. (2009) Soil organic carbon pools in the northern circumpolar permafrost region. *Global Biogeochem Cycles* 23(2):1–11.
2. Schuur EAG, et al. (2015) Climate change and the permafrost carbon feedback. *Nature* 520(7546):171–179.
3. Euskirchen ES, Bret-Harte MS, Scott GJ, Edgar C, Shaver GR (2012) Seasonal patterns of carbon dioxide and water fluxes in three representative tundra ecosystems in northern Alaska. *Ecosphere* 3(1):4.
4. Mack MC, Schuur EAG, Bret-Harte MS, Shaver GR, Chapin FS, III (2004) Ecosystem carbon storage in arctic tundra reduced by long-term nutrient fertilization. *Nature* 431(7007):440–443.
5. Webb EE, et al. (2016) Increased wintertime CO2 loss as a result of sustained tundra warming. *J Geophys Res Biogeosci* 121:249–265.
6. Barichivich J, et al. (2013) Large-scale variations in the vegetation growing season and annual cycle of atmospheric CO2 at high northern latitudes from 1950 to 2011. *Glob Change Biol* 19(10):3167–3183.
7. Graven HD, et al. (2013) Enhanced seasonal exchange of CO2 by northern ecosystems since 1960. *Science* 341(6150):1085–1089.
8. Forkel M, et al. (2016) Enhanced seasonal CO2 exchange caused by amplified plant productivity in northern ecosystems. *Science* 351(6274):696–699.
9. Piao S, et al. (2008) Net carbon dioxide losses of northern ecosystems in response to autumn warming. *Nature* 451(7174):49–52.
10. Parazoo NC, et al. (May 12, 2011) Moist synoptic transport of CO2 along the mid-latitude storm track. *Geophys Res Lett*, 10.1029/2011GL047238.
11. Sweeney C, et al. (2015) Seasonal climatology of CO2 across North America from aircraft measurements in the NOAA/ESRL Global Greenhouse Gas Reference Network. *J Geophys Res* 120(10):5155–5190.
12. Orbe C, et al. (2015) Air-mass origin in the arctic. Part I: Seasonality. *J Clim* 28(12): 4997–5014.
13. Euskirchen ES, Edgar CW, Turetsky MR, Waldrop MP, Harden JW (2014) Differential response of carbon fluxes to climate in three peatland ecosystems that vary in the presence and stability of permafrost. *J Geophys Res* 119(8):1576–1595.
14. Parazoo NC, et al. (2013) Interpreting seasonal changes in the carbon balance of southern Amazonia using measurements of XCO2 and chlorophyll fluorescence from GOSAT. *Geophys Res Lett* 40(11):2829–2833.
15. Oleson KW, et al. (2013) Technical description of version 4.5 of the Community Land Model (CLM). (Natl Cent Atmos Res, Boulder, CO).
16. Koven CD, et al. (2013) The effect of vertically-resolved soil biogeochemistry and alternate soil C and N models on C dynamics of CLM4. *Biogeosciences* 10(11):7109–7131.
17. Swenson SC, Lawrence DM, Lee H (2012) Improved simulation of the terrestrial hydrological cycle in permafrost regions by the Community Land Model. *J Adv Model Earth Syst* 4(3):8002–8016.
18. Le Quere C, et al. (2015) Global carbon budget 2014. *Earth Syst Sci Data* 7(1):47–85.
19. Koven CD, Lawrence DM, Riley WJ (2015) Permafrost carbon-climate feedback is sensitive to deep soil carbon decomposability but not deep soil nitrogen dynamics. *Proc Natl Acad Sci USA* 112(12):3752–3757.
20. Lawrence DM, Koven CD, Swenson SC, Riley WJ, Slater AG (2015) Permafrost thaw and resulting soil moisture changes regulate projected high-latitude CO2 and CH4 emissions. *Environ Res Lett* 10(9):094011.
21. Karion A, et al. (2015) Investigating Alaskan methane and carbon dioxide fluxes using measurements from the CARVE tower. *Atmos Chem Phys Discuss* 15(23):34871–34911.
22. Nassar R, Sioris CE, Jones DBA, McConnell JC (2014) Satellite observations of CO2 from a highly elliptical orbit for studies of the Arctic and boreal carbon cycle. *J Geophys Res* 119(5):2654–2673.
23. Ciais P, et al. (2014) Current systematic carbon-cycle observations and the need for implementing a policy-relevant carbon observing system. *Biogeosciences* 11: 3547–3602.
24. Hammerling DM, Kawa SR, Schaefer K, Doney S, Michalak AM (2015) Detectability of CO2 flux signals by a space-based lidar mission. *J Geophys Res Atmos* 120(5):1794–1807.
25. Schaefer K, Zhang T, Bruhwiler L, Barrett AP (2011) Amount and timing of permafrost carbon release in response to climate warming. *Tellus* 63B(2):165–180.
26. Koven CD, Riley WJ, Stern A (2012) Analysis of permafrost thermal dynamics and response to climate change in the CMIP5 Earth System Models. *J Clim* 26(6): 1877–1900.
27. Hicks Pries CE, et al. (2015) Decadal warming causes a consistent and persistent shift from heterotrophic to autotrophic respiration in contrasting permafrost ecosystems. *Glob Chang Biol* 21(12):4508–4519.
28. Zona D, et al. (2016) Cold season emissions dominate the Arctic tundra methane budget. *Proc Natl Acad Sci USA* 113(1):40–45.
29. Miller CE, Dinardo SJ (2012) CARVE: The Carbon in Arctic Reservoirs Vulnerability Experiment. *Proceedings of the IEEE Aerospace Conference* (IEEE, Big Sky, MT).
30. Chang RYW, et al. (2014) Methane emissions from Alaska in 2012 from CARVE airborne observations. *Proc Natl Acad Sci USA* 111(47):16694–16699.
31. Karion A, et al. (2013) Long-term greenhouse gas measurements from aircraft. *Atmos Meas Tech* 6(3):511–526.
32. Kuze A, Suto H, Nakajima M, Hamazaki T (2009) Thermal and near infrared sensor for carbon observation Fourier-transform spectrometer on the Greenhouse Gases Observing Satellite for greenhouse gases monitoring. *Appl Opt* 48(35):6716–6733.
33. Wunch D, et al. (2013) The covariation of Northern Hemisphere summertime CO2 with surface temperature in boreal regions. *Atmos Chem Phys* 13(18):9447–9459.
34. O'Dell CW, et al. (2012) The ACOS CO2 retrieval algorithm – Part 1: Description and validation against synthetic observations. *Atmos Meas Tech* 5(1):99–121.
35. Oda T, Maksyutov S (2011) A very high-resolution (1 km x 1 km) global fossil fuel CO2 emission inventory derived using a point source database and satellite observations of nighttime lights. *Atmos Chem Phys* 11(2):543–556.
36. Takahashi T, et al. (2009) Climatological mean and decadal change in surface ocean pCO2, and net sea–air CO2 flux over the global oceans. *Deep Sea Res Part 2 Top Stud Oceanogr* 56(8):554–577.

# Supporting Information

## Parazoo et al. 10.1073/pnas.1601085113

### SI Text

**S1: Observed $CO_2$.** CARVE campaign flights are conducted aboard a National Aeronautics and Space Administration C-23 Sherpa aircraft (29). $CO_2$ data were collected in Alaska for a period of 2 wk/mo from May to September of 2012 and from April to October of 2013, with 4–10 flights per campaign and 75 total tracks collected from 2012 to 2013. Surveys are conducted in the lowest 500 m of the atmosphere to target $CO_2$ exchange near the surface, with frequent vertical profiles to characterize gradients across the planetary boundary layer and regional budgets (Fig. S1). We use the merged product that combines measurements from NOAA and Harvard University Picarro instruments, with calibration periods in the Harvard instrument gap-filled using the NOAA instrument (30).

ACG is based on a collaboration between the US Coast Guard in Kodiak, AK and the NOAA Earth System Research Laboratory (NOAA/ESRL) Global Greenhouse Gas Reference Network to make flights as often as every 2 wk between Kodiak, AK and Barrow, AK (31). High-resolution $CO_2$ in situ concentration data were collected across more than 50 flights and an average of three vertical profiles per flight in the ML and FT from 2009 to 2013 from early March to late November (Fig. S2). These flights include frequent profiles at Barrow, AK, with coverage up to 82° N over the Arctic Ocean, and as far as the west coast of Alaska and east to Prudhoe Bay. ACG typically measures vertical profiles over boreal and Arctic Alaska on the same day.

PFA is based on high-resolution $CO_2$ flask concentration data collected by NOAA/ESRL at 12 different altitudes (500–8,000 masl) over the PFA Research Range northeast of Fairbanks, AK (roughly centered at 65.07° N, 147.29° W) every 2–4 wk since 2000. PFA data have been collected year-round to resolve the entire annual cycle of $CO_2$.

GOSAT has produced global measurements of $XCO_2$ since June of 2009 (32) and showed good agreement of seasonal and interannual $XCO_2$ variability compared with northern latitude surface measurements (33). $XCO_2$ retrievals are taken from the National Aeronautics and Space Administration ACOS full physics retrieval algorithm (34), version B3.5, which when aggregated over the growing season, provides high spatial coverage throughout the ABZ (Fig. S3), including partial coverage of shoulder seasons in spring and fall and full coverage of the growing season (April to September). In Alaska (55° N to 72° N, 170 ° W to 140° W), on average, we obtain 274 samples (~10.5-km footprints) per year from 2009 to 2013. Coverage peaks in summer (89 samples in June; 1–5 d average sampling interval), decreases toward shoulder seasons (10–20 samples), and dips in July (10 samples; 2–5 d) when a higher fraction of data are lost because of cloud cover. In the pan-Arctic (55° N to 72° N, 180 ° W to 180° E), we obtain 4,000–5,000 samples per year with similar seasonal distribution as in Alaska.

All aircraft datasets are filtered for biomass burning using onboard CO measurements and a high CO screen of 150 ppb and then, separated into ML and FT bins to examine local vs. long-range effects on $CO_2$ seasonality. We average all available data in the lowest 3 km asl (>700 mb) for the ML and from 3 to 7 km asl (700–500 mb) for the FT, noting that the approximate ML sampling altitude below 3 km varies across datasets (e.g., 0.6, 1.4, and 1.4 km asl for CARVE, ACG, and PFA, respectively, from July to August of 2012). Fall and spring zero crossing days, representing transitions between growing season carbon uptake and cold season emissions, are calculated using linear interpolation between adjacent monthly averaged $CO_2$ observations that occur on opposite sides of the zero crossing line created by removing the long-term trend. GOSAT collects data only through October at these high latitudes, and hence, we do not report a zero crossing for $XCO_2$. The long-term trend is determined using background observations at the Mauna Loa Observatory from 2009 to 2013, with high-frequency (seasonal and higher) variability removed by applying a low-pass zero-phase filter on monthly means using an infinite impulse response (IIR) filter of order six and cutoff frequency of 0.1.

On average, our vertical binning criteria for separating airborne data into the ML (lowest 3 km asl; >700 mb) and FT (3–7 km asl; 700–500 mb) decouple the surface from higher altitudes (Fig. S4). The layer between 2 and 3 km represents a residual layer with enhanced sensitivity to local processes depending on vertical mixing. In some years (e.g., 2013), it leads to more homogeneous profiles.

We investigate the effect of diurnal variability in Alaskan $CO_2$ exchange on diurnal sampling biases in ML data by analyzing $CO_2$ seasonal cycles using morning (8–12 LST; 25% of all data), afternoon (12–16 LST; 50% of data), and early evening (16–20 LST; 25% of data) averaging bins for CARVE (Fig. S5). The results show weak variability in the shape and duration of growing season drawdown, with the exception of strong ML drawdown in early evening and strong enrichment in morning and afternoon periods in 2013. Overall, the diurnal cycle has a small effect on the vertical distribution, vertical gradient, or shape of the $CO_2$ seasonal cycle.

Comparison of monthly $CO_2$ averages across airborne and satellite datasets in Alaska shows high consistency of seasonal and interannual variability and long-term growth (Fig. S7), including similar timing of peak summer depletion (July/August) and peak spring enrichment (April). This comparison also shows stronger variability in ML averages than in FT and column averages, with strongest summer depletion and spring enrichment in the ML and weakest in the column. Some years show similar variability in the ML and FT (2010), indicating enhanced coupling across the vertical column, whereas other years are more divergent (2012), indicating reduced coupling. Each platform and each underlying sampling strategy provide an important strength needed to characterize different characteristics of the Alaskan $CO_2$ seasonal cycle. PFA captures the full annual cycle within the continental interior, CARVE and ACG capture spatial variability during the growing season, and CARVE provides high-quantity measurements and captures high-frequency time and space variations near the surface within the continental interior. Each platform also has an important weakness. PFA does not capture spatial heterogeneity, ACG and CARVE do not sample thoroughly or consistently during wall and winter, ACG lacks continental sampling coverage and measurement quantity, and CARVE lacks longevity over multiple years of our study period.

Different observing strategies impact estimates of seasonal $CO_2$ structure and hence, our interpretation of seasonal cycle dynamics. Similarities and differences in seasonal cycle characteristics across datasets are best illustrated by comparing 5-y detrended seasonal composites (Fig. 1 *A* and *B*). With respect to seasonal amplitude, we find good agreement across datasets in the magnitude of the FT summer minimum (−7 ppm) and spring ML and FT maximum (+6 ppm) but an earlier and more persistent minimum in PFA and CARVE (July/August) compared with ACG (August) and earlier spring maximum in PFA and ACG (April) compared with CARVE (April/May). With respect to carbon uptake period, ACG and PFA show similar timing of

ML and FT spring zero crossing in early June, whereas CARVE is delayed to mid-June. Only PFA and CARVE resolve ML fall zero crossing in late September, with CARVE 1–2 wk earlier than PFA and both with higher enrichment rates compared with ACG. Only PFA resolves FT fall zero crossing, which is delayed by 1 mo compared with the ML in late October. With respect to interannual variability, all datasets show the strongest interannual variability in summer and fall and the weakest interannual variability in spring.

Averaging across datasets from 2009 to 2013 combines unique strengths across observing systems to better characterize seasonal cycle behavior at different spatial scales (Fig. 1). In the FT, we find a seasonal amplitude of 13.6 ± 3.5 ppm and a carbon uptake period of 161 ± 24.3 d, including a spring zero crossing Julian date of 159 ± 9.24 d and a fall zero crossing of 320 ± 18.9 d. By contrast, the ML shows a 28% stronger amplitude (17.4 ± 3.5 ppm) and a 15% shorter period (137 ± 16.4 d) driven by 3–4 wk earlier fall zero crossing date (294 ± 15.1 d). Although the ML shows enhanced rates of spring depletion (13.1 vs. 10.4 ppm from May to July) and fall enrichment (12.7 vs. 8.2 ppm from August to November), only fall enrichment is associated with a significant difference in zero crossing date (26 d in fall vs. 2 d in spring).

**S2: Land and Atmospheric Simulations.** Atmospheric $CO_2$ is simulated using the GEOS-Chem global tracer transport model (14) forced by assimilated meteorological fields and surface $CO_2$ flux from land, ocean, and fossil fuel sources. All GEOS-Chem runs are forced with observed meteorology from the Modern-Era Retrospective Analysis for Research and Applications (data available at disc.sci.gsfc.nasa.gov/mdisc/). GEOS-Chem is spun up from 2000 to 2008 using time-varying winds and $CO_2$ flux to force interannual variability and establish hemispheric gradients. Land $CO_2$ flux is prescribed using two configurations of the CLM4.5.

CLM4.5 includes a basic set of permafrost processes to allow projection of permafrost carbon–climate feedbacks, including vertically resolved soil organic matter dynamics and soil hydrology and snow schemes (15–17). We use two types of simulations in this study: (*i*) present day runs, which are forced by observed meteorological forcing through 2013 (18), and (*ii*) historical and future runs, which are forced by historical and future warming scenarios (19). All CLM4.5 runs are forced with observed meteorology from CRUNCEP analysis (data available at dods.ipsl.jussieu.fr/igcmg/IGCM/BC/OOL/OL/CRU-NCEP/).

***Present day runs.*** The first set of experiments focuses on present day simulations from 2009 to 2013. GEOS-Chem is forced by year-specific winds and $CO_2$ flux to best represent observed conditions and interannual variability. Monthly land flux is prescribed using CLM4.5 forced by year-specific CRUNCEP analysis (18). Monthly fossil fuels are taken from ODIAC (35) and air–sea exchange is from climatological surface ocean partial pressure of $CO_2$ ($pCO_2$) (36). Three variants are considered: (*i*) CONTROL, a baseline run with all fluxes turned on; (*ii*) ALASKA-OFF, an Arctic influence run in which Alaskan fluxes are set to zero for the domain (55° N to 72° N, 170° W to 140° W); and (*iii*) ARCTIC-OFF, the long-range transport run where Arctic fluxes are set to zero for the domain (55° N to 90° N, 180° W to 180° E).

***Historical and future runs.*** The second set of experiments is based on CLM4.5 fluxes from historical and future warming scenarios. Atmospheric simulations are forced by time-varying winds from Modern-Era Retrospective Analysis for Research and Applications from 2000 to 2010 and use six sets of decadal CLM4.5 fluxes for present day (HIST, 1990–2010) and future (15YR, 2005–2015; 30YR, 2020–2030; 50YR, 2040–2050; 100YR, 2090–2100; and 200YR, 2190–2200) scenarios. These scenarios are further divided into simulations to test $CO_2$ sensitivity to flux changes in Alaska (ALASKA-ON), in the Arctic (ARCTIC-ON), and at global scale (GLOBAL-ON). To isolate sensitivity to biology and permafrost thaw in future warming scenarios, GEOS-Chem is initialized with January of 2010 $CO_2$ and run without fossil and ocean fluxes.

CLM4.5 is configured as described in two recent permafrost studies (19, 20) using climate runs in which modeled photosynthesis is driven by constant preindustrial $CO_2$. From 1850 to 2005, CLM4.5 is forced with observed meteorology from the CRUNCEP dataset. For the period 2005–2300, an anomaly forcing method is used to repeatedly force CLM4.5 future runs with the observed meteorological forcing from CRUNCEP for the period 1996–2005, with monthly anomalies added based on a single ensemble member from a CCSM4 RCP8.5 simulation. The period from 1996 to 2015 represents a base climatological period used for calculating monthly anomalies, with a 20-y record chosen to minimize large anomalies in the first few years. This process is repeated for all variables and all times from 2006 to 2300 (constantly cycling through the same 1996–2005 observed data).

We use two examples to show the use of this method for future simulations. For a simulation on January 31, 2006, the temperature forcing is calculated by taking the CRUNCEP temperature value on January 31, 1996 and adding the monthly anomaly from the CCSM4 simulation for January of 2006. In this case, because January of 2006 overlaps the base climatological period, the anomaly value is likely close to zero. For a simulation on January 31, 2106, the temperature forcing is calculated by taking the CRUNCEP temperature value on January 31, 1996 and adding the monthly anomaly from the CCSM4 simulation for January of 2106. In this case, the anomaly value is likely to be significantly different from zero, because the anomaly represents the difference between RCP8 simulations in 2106 and base climatology in 2006.

We note several limitations in this approach: (*i*) we implicitly assume that the diurnal cycle amplitude and submonthly variability are not trending, and (*ii*) we are evaluating climate change from one model and one ensemble member and thus, have not considered the range of future climate change projections on CLM4.5 fluxes.

We consider two scenarios for permafrost thaw. The first, denoted FUTURE-DEEP, assumes that deep permafrost carbon is active (19). In the second, denoted FUTURE-SHALLOW, deep soil decomposition is disabled by varying a parameter $Z_\tau$ in CLM4.5, which controls decomposition rates as a function of soil depth. These experiments serve to decouple changing dynamics of surface soils from deep soils and allow isolation of the potential contribution from permafrost layers (19).

Because we are interested in identifying the detectability of climate-driven signals in the absence of $CO_2$ fertilization effects, historical and future simulations are based on climate runs in which modeled photosynthesis is driven by constant preindustrial $CO_2$. The climate only runs shift the ABZ from near carbon-neutral conditions in 1990–2010 to a strong source (1.3 Pg C $y^{-1}$) in 100–200 y (Fig. S6*A*). For comparison, simulations with $CO_2$ fertilization leads to a similar increase in emissions over the next 200 y but with increased amplitude of seasonal exchange because of stronger growing season uptake and enhanced winter respiration (Fig. S6*B*).

**S3: Long-Range Transport.** Simulations with global fluxes (CONTROL) slightly overestimate observed seasonal amplitude in the ML (Fig. S8*B*) (19.3 vs. 17.4 ppm) and FT (Fig. S8*C*) (15.2 vs. 13.6 ppm) and delay fall zero crossing by 16 and 3 d, respectively. Zeroing Alaska $CO_2$ fluxes (ALASKA-OFF) yields little change in the FT; in the ML, zeroing Alaska $CO_2$ fluxes reduce early summer depletion (2–3 ppm in Jun and July) and delays fall zero crossing by an additional week. Zeroing all Arctic fluxes (ARCTIC-OFF) drives significant reductions to seasonal amplitude in the ML and FT (~30% compared with CONTROL) and delays ML fall zero crossing by another week. Combined transport from the pan-Arctic and low latitudes accounts for 88% of ML amplitude

in CONTROL (67% from low latitudes and 21% from pan-Arctic) and 96% in the FT (73% from low latitudes and 23% from pan-Arctic). We find very little amplitude contribution from Alaskan fluxes (≤10%).

**S4: Interannual Variability.** The observed vertical gradient also exhibits interannual variability in summer $CO_2$ minima ($\sigma = 0.80$ ppm) (Fig. S9*A*). CONTROL runs reproduce much of the observed variability during summer. Although slightly weaker than observed ($\sigma = 0.60$ ppm), simulated variability exceeds the RMSE (0.40 ppm) and shows a positive relationship to summer $CO_2$ fluxes in CLM4.5 ($y = 6.67x + 2.29$ ppm/g C $m^{-2}$ $d^{-1}$; $r = 0.88 \pm 0.275$ ($p = 0.049$)) (Fig. S9*B*). The relationship is positive but less significant in fall (Fig. S9*C*). Comparison with eddy covariance $CO_2$ flux measurements suggests that these relationships are linked to climate variability and in particular, reflect high sensitivity in permafrost ecosystems to summer warming (3). For example, slightly reduced $CO_2$ depletion in 2013 (−2.3 ppm compared with the 2009–2013 mean of −2.6 ppm) is consistent with increasing source activity in permafrost ecosystems during hot, dry summers. In contrast, the significantly enhanced summer $CO_2$ minimum in 2012 (−3.9 ppm) is consistent with net $CO_2$ sink activity in 2012 when air temperature and precipitation were near long-term means. These results highlight the importance of sustained airborne observations over multiple consecutive years.

We also find strong variability in observed fall $CO_2$ maxima ($\sigma = 0.74$ ppm), but observed variability is poorly reproduced by CONTROL simulations ($\sigma = 0.24$ ppm), which also show much weaker sensitivity to $CO_2$ fluxes in CLM4.5 compared with summer ($y = 2.89x + 1.05$ ppm/g C $m^{-2}$ $d^{-1}$). Although these data could signal $CO_2$ flux anomalies in fall, it is unclear from our simulations whether $CO_2$ flux variations are detectable in atmospheric $CO_2$ observations in the present climate.

**S5: Climate-Induced $CO_2$ Flux Projections.** This section discusses briefly climate change impacts outside on Alaskan $CO_2$ seasonality. In contrast to high latitudes, midlatitudes show reduced summer uptake and winter emissions with climate change (Fig. S10 *A* and *B*). Pan-Arctic climate change (ARCTIC-ON) drives an additional 0.3- to 0.8-ppm summer $CO_2$ depletion and 2–3 ppm winter enrichment (Fig. S10 *C* and *D*), whereas global climate change (GLOBAL-ON) drives an additional 1-ppm summer depletion, despite reduced uptake in lower latitudes, with negligible changes in winter enrichment (Fig. S10*E*). A confounding effect is that transport from reduced uptake regions in lower latitudes leads to a lower rate of FT $CO_2$ depletion compared with the ML (Fig. S10*H*).

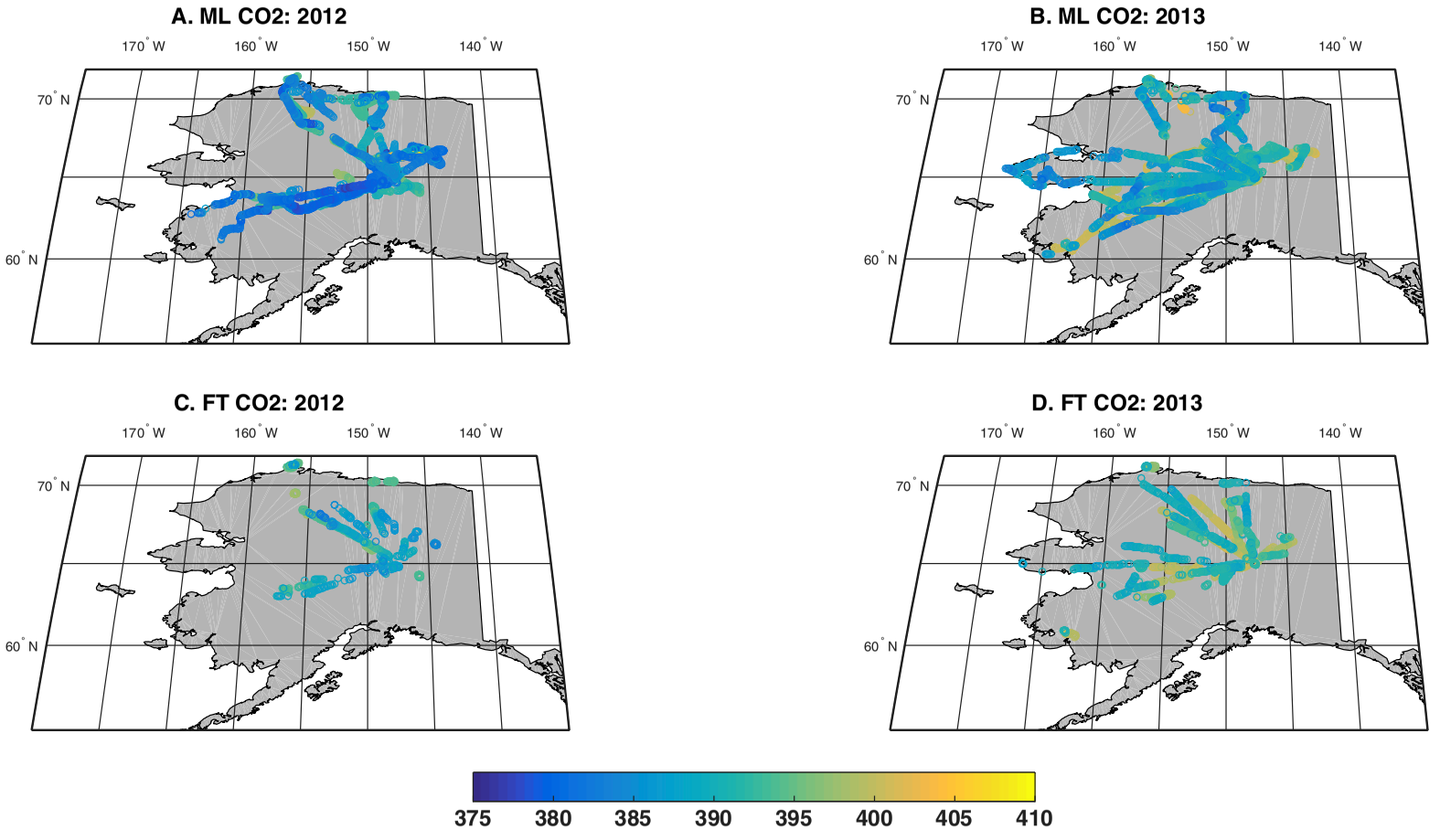


**Fig. S1.** Maps of growing season (June to August) averaged $CO_2$ from 2012 to 2013 for CARVE divided into (*A* and *B*) ML (0–3 km asl) and (*C* and *D*) FT (3–7 km asl).

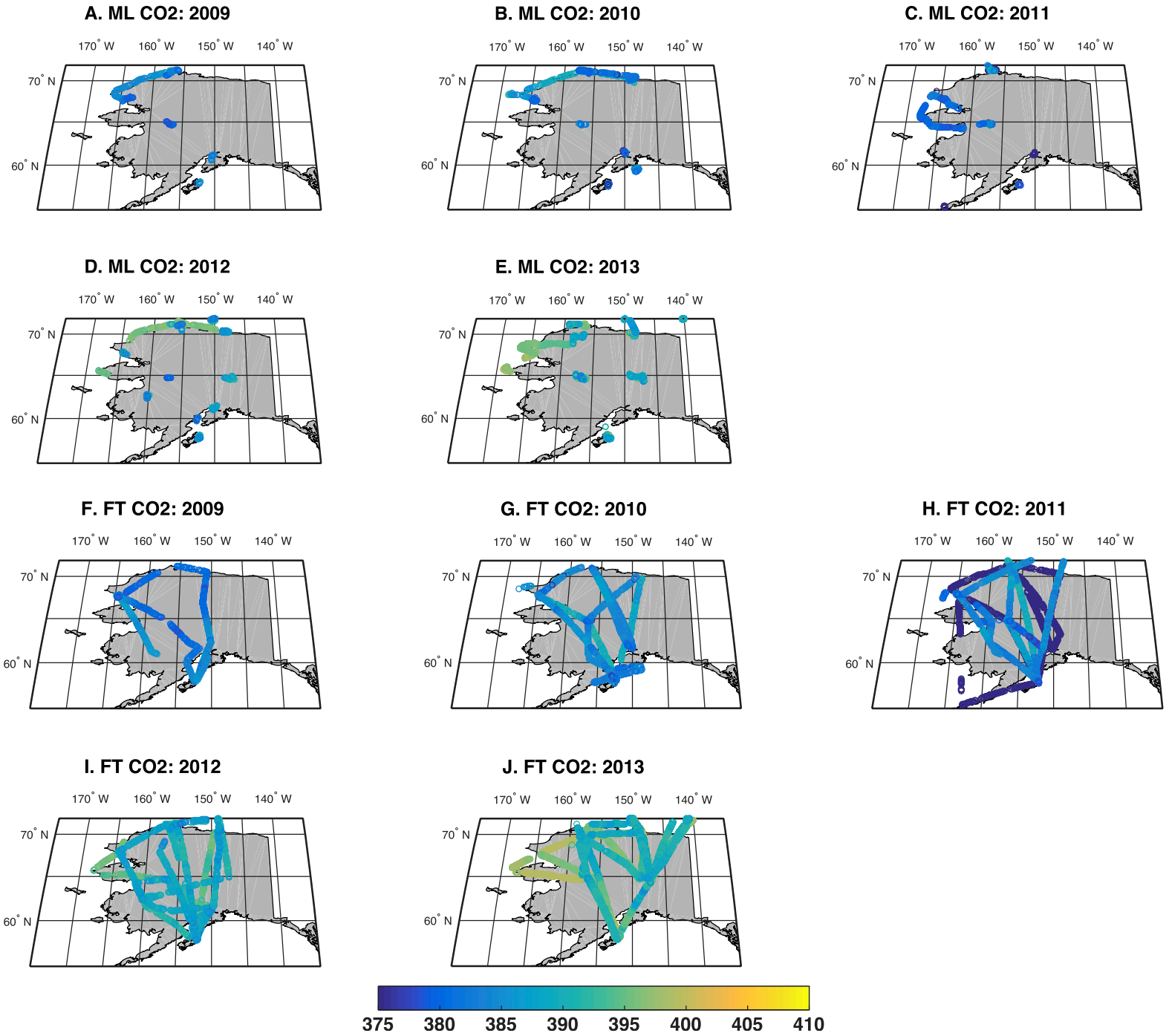


**Fig. S2.** Maps of growing season (June to August) averaged $CO_2$ from 2009 to 2013 for ACG divided into (*A*–*E*) ML (0–3 km asl) and (*F*–*J*) FT (3–7 km asl).

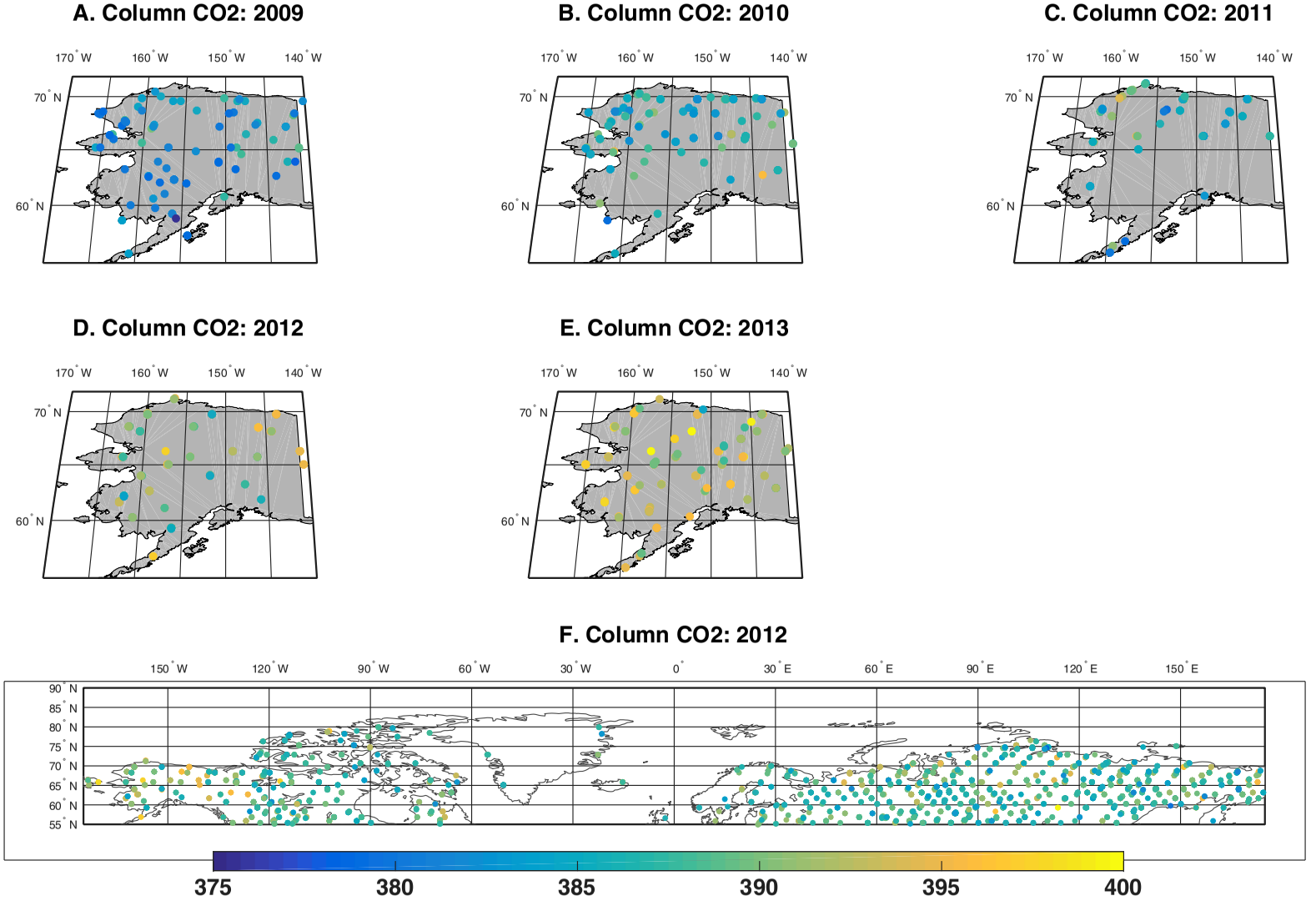


**Fig. S3.** Maps of growing season (June to August) averaged column $CO_2$ from 2009 to 2013 for GOSAT for Alaska (*A–E*) and pan-Arctic (*F*).

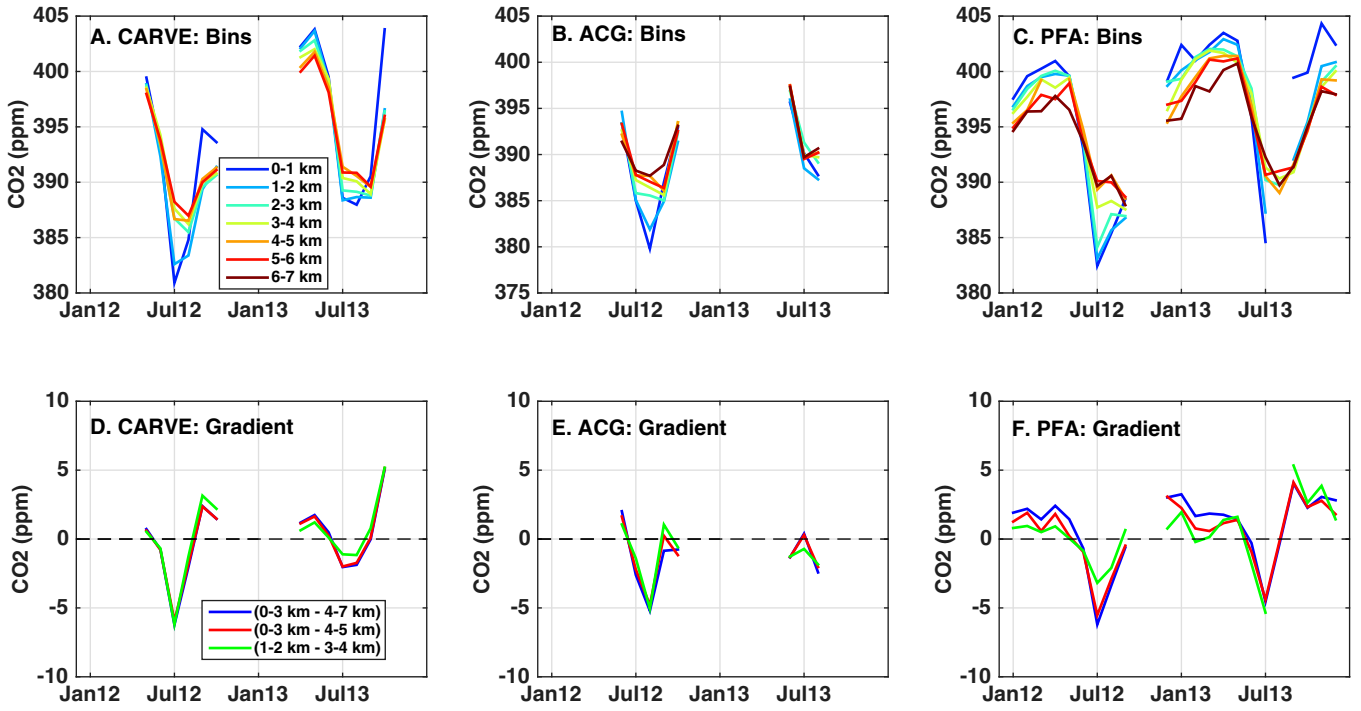


**Fig. S4.** $CO_2$ seasonal cycles for (*A* and *D*) CARVE, (*B* and *E*) ACG, and (*C* and *F*) PFA separated into 1-km vertical bins from the surface to 7 km (*A*–*C*) and corresponding vertical gradients for various ML and FT average bins (*D*–*F*).

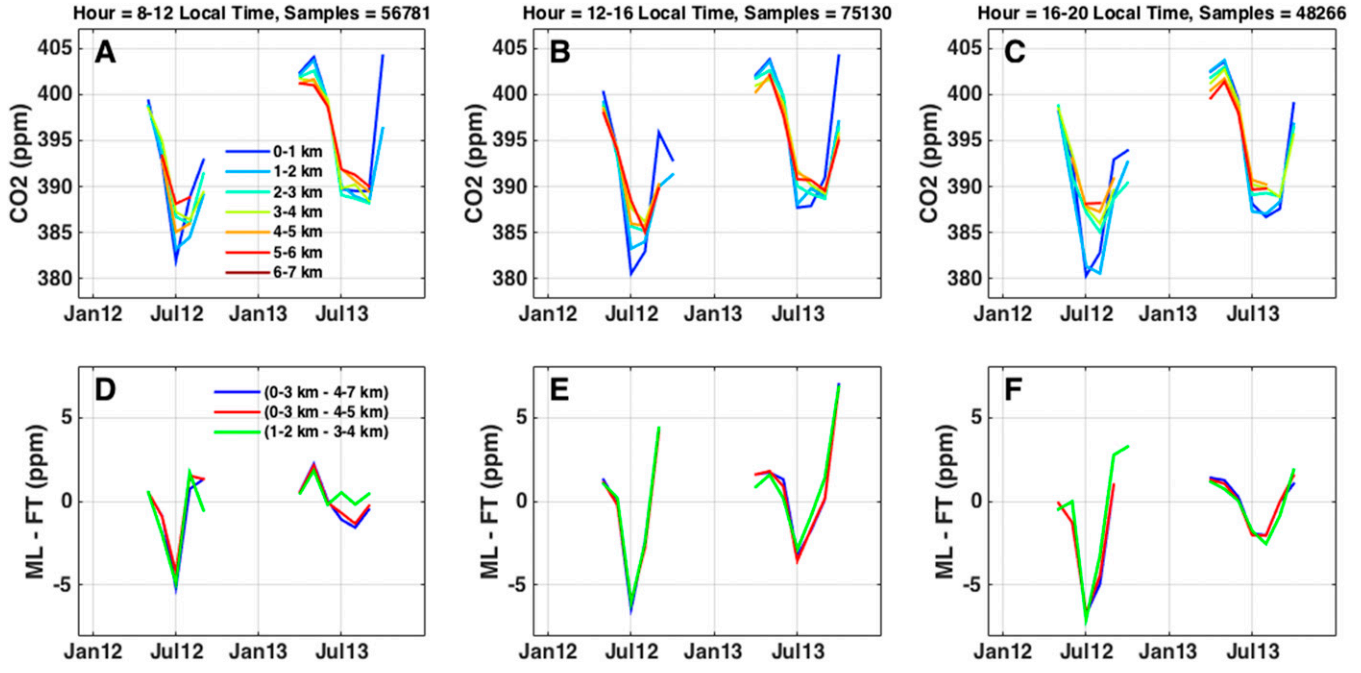


**Fig. S5.** $CO_2$ seasonal cycles for CARVE separated into diurnal bins for (*A* and *D*) 8–12 local time, (*B* and *E*) 12–16 local time, and (*C* and *F*) 16–20 local time, separated into 1-km vertical bins from the surface to 7 km (*A*–*C*) and corresponding vertical gradients for various ML and FT average bins (*D*–*F*).

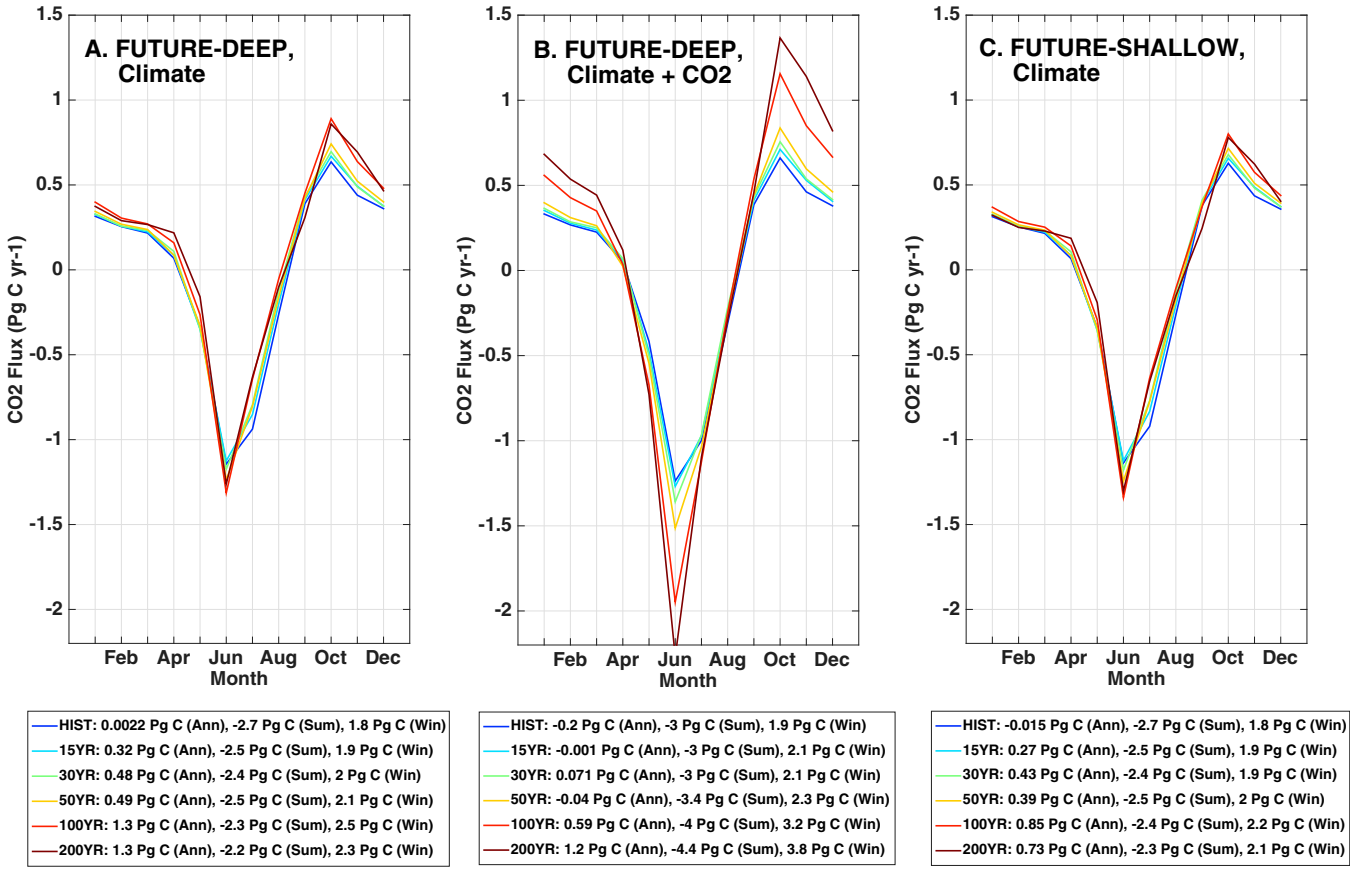


**Fig. S6.** Seasonal $CO_2$ flux changes under future warming scenarios over the next 200 y using climate runs with and without $CO_2$ fertilization. Scenarios include (*A*) deep soils (FUTURE-DEEP; $Z_\tau = 10$ m) without $CO_2$ fertilization, (*B*) deep soils with $CO_2$ fertilization, and (*C*) shallow soils (FUTURE-SHALLOW; $Z_\tau = 0.5$ m) without $CO_2$ fertilization. Results are shown for pan-Arctic–scale emissions (ARCTIC-ON). Future $CO_2$ exchange is reported at annual, summer, and fall timescales below figures.

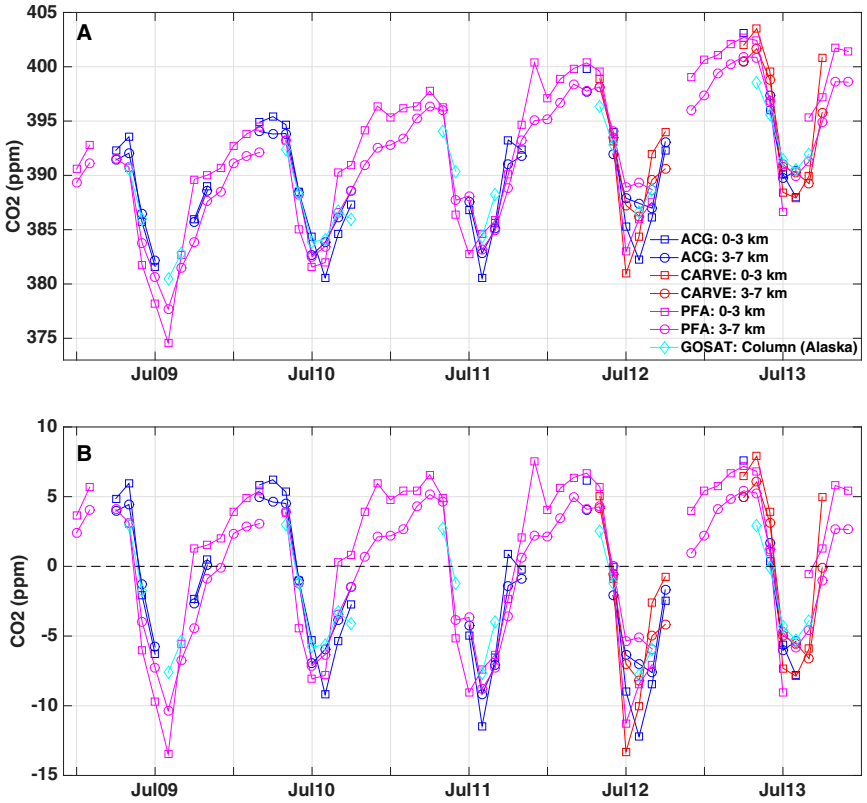


**Fig. S7.** Alaskan $CO_2$ observations time series for 2009–2013 for airborne and satellite observations. Airborne observations are averaged into altitude bins for the ML (0–3 km asl; □) and FT (3–7 km asl; ○). Column observations are averaged over Alaska (cyan). Results are shown for (*A*) raw $CO_2$ and (*B*) detrended $CO_2$ for 2009–2013 based on Mauna Loa $CO_2$ trend over the same period.

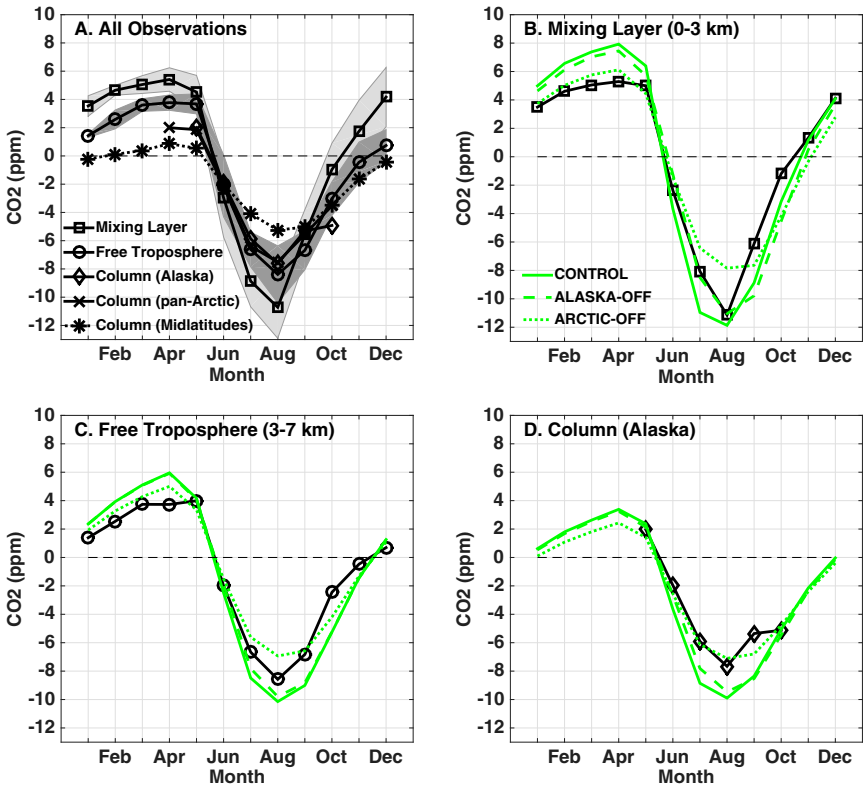


**Fig. S8.** Observed and simulated $CO_2$ seasonal cycles for airborne and satellite observations averaged from 2009 to 2013. Airborne data are monthly averages across PFA, CARVE, and ACG for ML (0–3 km asl; □) and FT (3–7 km asl; ○) bins. GOSAT data are column averages for Alaska (♢), pan-Arctic (55° N to 72° N; ×), and middle latitudes (30° N to 55° N; *). Shading is the monthly SD, representing interannual variability over 5 y. (*A*) Airborne and satellite observations. (*B–D*) Observed and simulated seasonal cycles for (*B*) ML, (*C*) FT, and (*D*) column. Simulations are from TRANSPORT experiments, including CONTROL (solid lines), ALASKA-OFF (dashed lines), and ARCTIC-OFF (dotted lines).

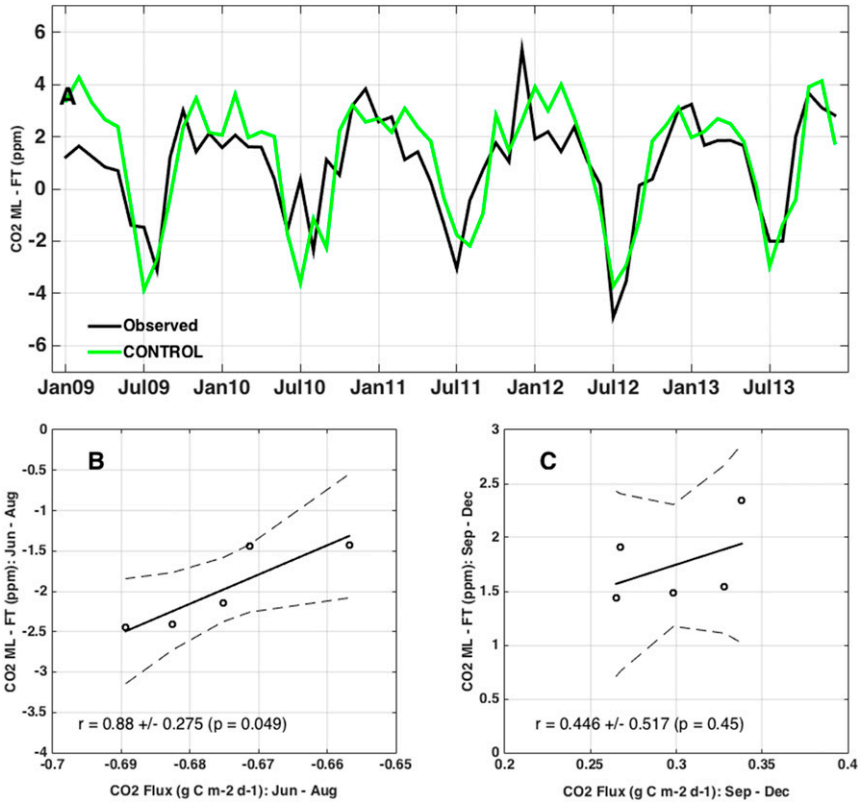


**Fig. S9.** $CO_2$ interannual variability and sensitivity to Alaska $CO_2$ flux. (*A*) Variability from 2009 to 2013 of the $CO_2$ vertical gradient (ML − FT) for combined airborne observations (black) and CONTROL simulations (green). Regression of CONTROL $CO_2$ against CLM4.5 $CO_2$ flux during (*B*) summer (June to August) and (*C*) fall/winter maximum (September to December). Pearson correlation coefficient and *P* value are also shown.

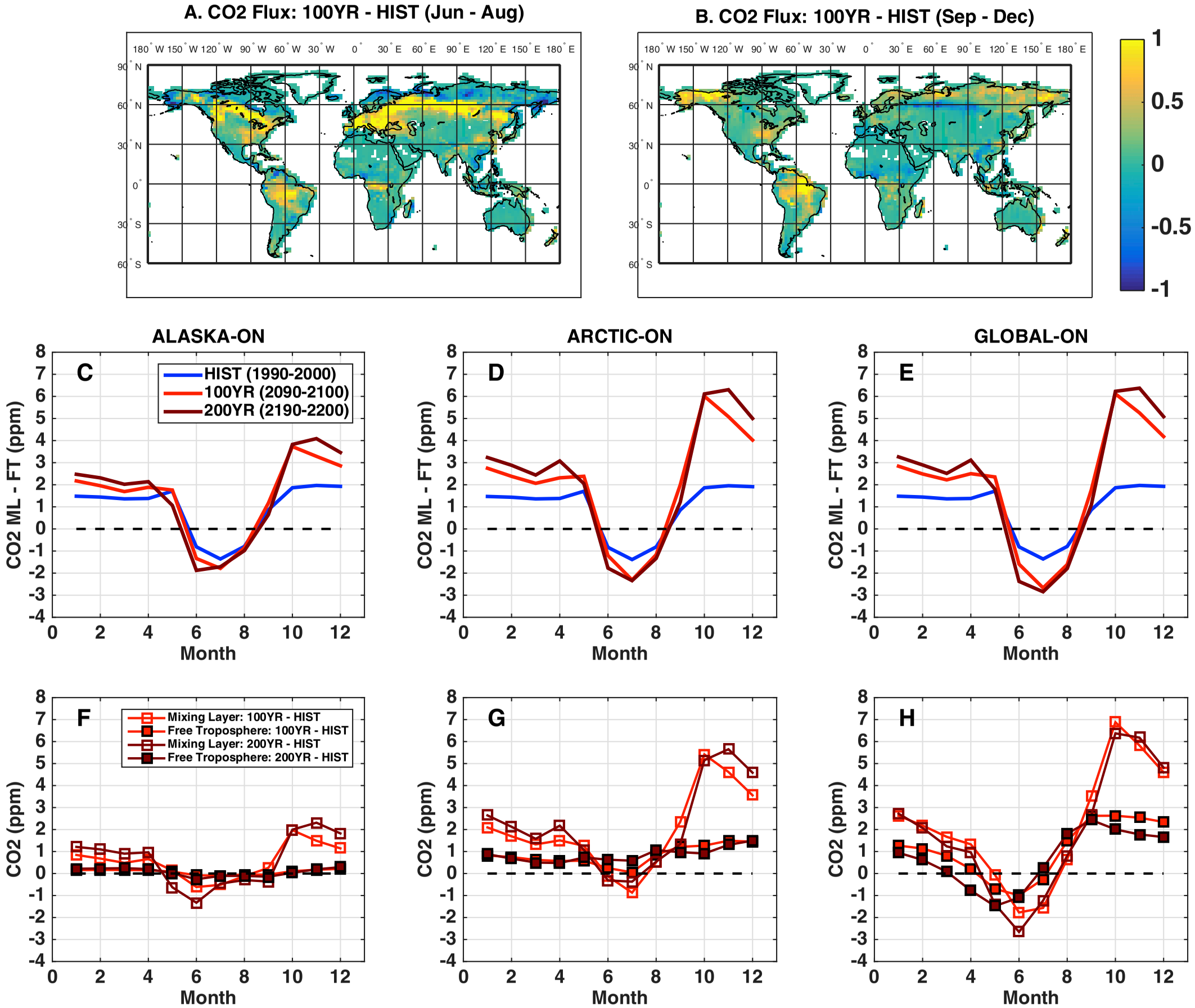


**Fig. S10.** Changes in $CO_2$ flux and atmospheric $CO_2$ for FUTURE-DEEP warming scenario over the next 100–200 y of $CO_2$ flux changes in 2100 (FUTURE1 – HIST) for CLM4.5 fixed carbon climate projections are shown for (*A*) summer (June to August) and (*B*) winter (September to December). $CO_2$ seasonal cycle changes in Alaska are shown for HIST (blue), FUTURE1 (light red), and FUTURE2 (dark red) using $CO_2$ flux scenarios for (*C* and *F*) ALASKA-ON, (*D* and *G*) ARCTIC-ON, and (*E* and *H*) GLOBAL-ON. $CO_2$ vertical gradient is shown in *C*–*E* (ML – FT) and shown for separate ML and FT bins in *F*–*H*.